Sensors & Actuators: B. Chemical 404 (2024) 135257

Contents lists available at ScienceDirect

Sensors and Actuators: B. Chemical

journal homepage: www.elsevier.com/locate/snb

Synergetic crystal phases of SnO_2/NiO heterostructure in an interconnected morphology for chemiresistive formaldehyde sensors

Jihyun Lee [a], Yu Jin Kim [a,b,*], Wooyoung Lee [a,**]

[a] Department of Materials Science and Engineering, Yonsei University, 50 Yonsei-ro, Seodaemun-gu, Seoul 03722, Republic of Korea
[b] KIURI Institute, Yonsei University, 50 Yonsei-ro, Seodaemun-gu, Seoul 03722, Republic of Korea

ARTICLE INFO

Keywords:
Metal oxide gas sensor
SnO_2/NiO heterostructure
SnO_2/NiO nanoparticle
Formaldehyde gas sensor
Formaldehyde sensing

ABSTRACT

A SnO_2/NiO heterostructure that is comprised of SnO_2 and NiO nanoparticles was designed and demonstrated an extremely high sensing response toward formaldehyde detection. A facile one-step blending process with a low operating temperature of 80 °C enables an interconnected morphology for the SnO_2/NiO heterostructure. Two particles were created in the morphology by encouraging the formation of crystal phases in each other, the synergetic crystal phases of the SnO_2/NiO heterostructure were generated with excellent crystallinity and high crystallite size and chemically constructed. The synergetic crystalline morphology facilitates adsorbed oxygen species on the SnO_2/NiO heterostructure to have effective chemical interaction with formaldehyde gas molecules in terms of not only surface and internal crystal structure but also electronic band structure. It thereby leads to an extremely high sensing response with a record value of 9121.74 in the detection of formaldehyde with a 10 ppm concentration. With the overwhelming response, the SnO_2/NiO heterostructure-based sensor device showed a transient response time within 3 s, a significant stable result in repeatability including reproducibility with ca. 2% loss in the gas ON-OFF level in the 50 cycles, long-term stability for 12 days, and ultra-exclusive selectivity result. Our work suggests a realization method to develop SnO_2/NiO heterostructure-based chemiresistive sensor with a superior sensing response, and thus it will be a leading research outcome in both communities of formaldehyde gas sensors and SnOx-based sensor devices.

1. Introduction

Tin(II) oxide (SnO_2) nanostructures have been extensively utilized as gas sensor materials and have been continuously developed as leading frameworks in the research community of gas sensors [1,2]. According to a report from the Web of Science in 2022, SnO_2 nanomaterials accounted for nearly 30% of usage in metal-oxide semiconductor gas sensors, establishing them as the most used materials [2]. SnO_2 is a tetragonal rutile structure and an n-type semiconductor with a wide band gap of 3.6 eV [3,4]. It has a crucial advantage for the dual valencies of Sn on the surface, which enables a reversible surface composition from stoichiometric surfaces with Sn^{4+} cations into a reduced surface with Sn^{2+} cations depending on the oxygen chemical potential [3,5]. The dual active sites on the surface of the SnO_2 facilitate to form chemically different adsorbed oxygen ions, i.e., O_2^-, O^-, and O^{2-} at different temperatures. Therefore, the surface characteristic of the SnO_2 allows a broad detection of various gases such as H_2S, CO, NOx, liquefied petroleum gas (LPG, mainly propane and butane), methanol, NH_3, and other gases at low concentrations [1,3,6].

With the SnO_2 advantages, other types of metal oxide can be incorporated into the SnO_2 structure to enhance its catalytic properties towards oxidation of target gas. Nickel oxide (NiO) is a representative metal oxide semiconductor and has great potential in oxidation catalytic activity [7–9]. Thus, a remarkable chemical interaction can be achieved between a substantial number of chemisorbed oxygen species and target gas in the SnO_2/NiO heterostructure. The adsorbed oxygen molecules on the surface of the heterostructure trap electrons that are released back to the conduction band of the SnO_2/NiO, generating chemisorbed oxygen species, and thus they attract and have chemical communication with the target gas molecules [10,11].

The SnO_2/NiO catalytic effect has been employed in the formaldehyde gas sensors. Meng's research group reported a NiO-SnO_2 microflower-based sensor that showed the high catalytic activity of NiO [12]. Sang's research team focused on establishing the catalytic

* Corresponding author at: Department of Materials Science and Engineering, Yonsei University, 50 Yonsei-ro, Seodaemun-gu, Seoul 03722, Republic of Korea.
** Corresponding author.
E-mail addresses: yujin.kim@yonsei.ac.kr (Y.J. Kim), wooyoung@yonsei.ac.kr (W. Lee).

https://doi.org/10.1016/j.snb.2023.135257
Received 8 September 2023; Received in revised form 26 December 2023; Accepted 28 December 2023
Available online 30 December 2023

oxidation of formaldehyde in the SnO_2/NiO heterostructure nanofibers [13]. Kumar's group developed SnO_2-decorated NiO nanoparticles and demonstrated their catalytic kinetics in formaldehyde adsorption-desorption [14]. The literatures have been dedicated to exploiting the catalytic synergy of SnO_2 and NiO structures, however, the sensing properties, particularly in terms of sensing response, showed a limited range of approximately between 30 to 40 in the detection of formaldehyde at a high concentration of 50 ppm or 100 ppm. It suggests that the development of SnO_2/NiO heterostructure-based formaldehyde gas sensors with a superior sensing response at low concentrations remains a challenging task.

In this work, we realized an extremely high formaldehyde gas sensor based on the SnO_2/NiO heterostructure and achieved a sensing response of 9121.74 in the detection of formaldehyde with a 10 ppm concentration. A facile one-step blending process provides an interconnected morphology that is blended with SnO_2 and NiO nanoparticles (NPs). SnO_2 and NiO encourage the formation of individual crystal phases each other in the morphology, creating a synergetic crystal structure. It thereby results in the ultra-high sensing property in the SnO_2/NiO heterostructure-based formaldehyde sensor device. To the best of our knowledge, the sensing response is a record value in the formaldehyde sensor community.

2. Experimental section

2.1. Chemicals

Tin(II) chloride dihydrate ($SnCl_2{\cdot}2\ H_2O$, $\geq$ 99.99% trace metals basis), nickel(II) chloride ($NiCl_2$, 99.99% trace metals basis), hexamethylenetetramine (HMTA, $\geq$ 99.0% ACS reagent), and α-terpineol (90% technical grade) were purchased from Sigma-Aldrich and used without further purification. Deionized water (di-water) was obtained from Millipore Milli-Q (18 mΩ cm) and used in all experiments as a solvent.

2.2. Synthesis of pure SnO_2, pure NiO, and SnO_2/NiO heterostructure NPs

For the synthesis of pure SnO_2 NPs, 2.5 mM of $SnCl_2{\cdot}2\ H_2O$ and 50 mM of HMTA (molar ratio: 1:20) were dissolved in di-water (80 mL). For the synthesis of NiO NPs, a proper amount of $NiCl_2$ (0.5, 1, 2, or 5 mM) was dissolved in di-water (80 mL) with 50 mM of HMTA. The SnO_2/NiO heterostructure NPs were synthesized with a molar ratio of 10:2, 5:2, 2.5:2, or 1.67:2 mM in the SnO_2:NiO blend. The two salts were dissolved in di-water (80 mL) with 50 mM of HMTA. All di-water solutions were blended at 80 ℃ for 24 h. After mixing, each blend of SnO_2, NiO, and SnO_2/NiO heterostructure resulted in a solution with yellow-brown, mint, and green precipitation, respectively. The precipitation was washed by di-water three times and the supernatant was removed by a centrifuge process (3900 rpm, 10 min). Finally, pure SnO_2, pure NiO, and SnO_2/NiO NP powders were obtained by calcination at 550 ℃ for 2 h under N_2 environment (Fig. S1) [15,16].

2.3. General characterization

Field-emission scanning electron microscope (FE-SEM, JSM-7001 F JEOL Ltd.) measurements were conducted to scan the surface morphology of the synthesized NPs. High-resolution transmission electron microscopy (HR-TEM) was performed using a JEM-ARM200F, NEOARM (JEOL Ltd.) equipment operating at 200 kV. X-ray diffraction (XRD) profiles were recorded by a SmartLab diffractometer (RIGAKU) with Cu Kα radiation ($\lambda = 1.541$ Å). The pure samples (SnO_2 and NiO) for the XRD measurement were prepared with a blend of HMTA. The surface chemical compositions of the NPs were obtained by X-ray photoelectron spectroscopy (XPS, K-alpha - Thermo U. K.) with a monochromatic Al Kα irradiation (1486.6 eV). UV–visible absorption spectra of the solutions (SnO_2, NiO, or SnO_2/NiO heterostructure precursors were diluted in di-water (initial synthesis state) and their synthesized powders in ethanol (final synthesis state) with a 0.025 mM concentration) were scanned using a V-650 spectrophotometer (JASCO Co.), and the background was corrected by air and di-water baseline. The functional groups in the pure SnO_2 and SnO_2/NiO heterostructure were identified by Fourier transform infrared (FT-IR) spectroscopy. The measurements were conducted using a Bruker VERTEX 70 spectrometer in transmission mode (KBr pellet) with a scan range of 3000 – 400 cm^{-1} (a resolution limit of 4 cm^{-1}). The electrical potential barrier including work function and valence band level information was analyzed by the measurement of ultraviolet photoelectron spectroscopy (UPS, AXIS SUPRA – Shimadzu Co.). The UPS measurement of step size is 1 meV and sensitivity is 106 cps at 120 meV resolution. Each sample bias of – 5 V was applied to observe the secondary electron cut-off.

2.4. Fabrication and measurement of pure SnO_2, pure NiO, and SnO_2/NiO heterostructure sensor devices

The SnO_2/NiO heterostructure sensor devices were fabricated on the interdigitated electrodes (IDEs) that were comprised of Cr (20 nm) and Pt (100 nm). The IDEs were patterned on a SiO_2/Si substrate (8.5 × 8.5 mm^2) using a lift-off method [17] and metal deposition was performed using a direct current magnetic sputtering system (a gap of electrodes: 5 μm). To create a SnO_2/NiO NP network, the heterostructure powders were blended with an α-terpineol binder. The mixture was spread on the IDEs with a flat surface and high adhesion. The SnO_2/NiO network-deposited IDE substrate was annealed at 600 ℃ for 1 h under N_2 environment to remove the binder residue and improve the stability of the film. For the pure SnO_2 and pure NiO sensor devices, the fabrication procedure was followed by the SnO_2/NiO heterostructure device in the same manner.

Gas sensing behaviors of pure SnO_2, pure NiO, and SnO_2/NiO heterostructure sensor devices were evaluated using a customized sensing measurement system with mass flow controllers (MFCs). The MFCs were connected to a tube furnace (quartz tube, 25 ∅ diameter) and four-channel gas lines (each line, 6 ∅ diameter), separately. The sensor device can be mounted into the tube furnace and it has a temperature controller to operate temperatures in a range of 200 - 500 ℃ (interval temperature of 50 °C and an error range of ±0.5 °C). The target gas was formaldehyde, which was a dry gas with a concentration of 10.9 μmol/mol with N_2 balance gas. For the sensitivity test as a function of target gas concentrations, various formaldehyde concentrations from 0.01 ppm to 10 ppm were applied with a dilution of the synthetic air (80% nitrogen and 20% oxygen, dry air). In the selectivity test, other test gases including formaldehyde (acetone (dry gas, concentration of 10.3 μmol/mol with N_2 balance gas), isoprene (dry gas, concentration of 101.8 μmol/mol with dry air balance gas), nitrogen dioxide (NO_2 – dry gas, concentration of 49.2 μmol/mol with dry air balance gas), xylene (dry gas, concentration of 10.3 μmol/mol with dry air balance gas), hydrogen (H_2 – dry gas, concentration of 9.94 μmol/mol with dry air balance gas), methane (CH_4 – dry gas, 9.92 μmol/mol with dry air balance gas), carbon dioxide (CO_2 – dry gas, concentration of 193.2 μmol/mol with dry air balance gas), carbon monoxide (CO – dry gas, concentration of 10.7 μmol/mol with N_2 balance gas), and ethyl benzene (dry gas, concentration of 48.8 μmol/mol with dry air balance gas)) were also balanced with the synthetic air to test the sensing response in a concentration of 10 ppm (all test gases were dry gas). The total gas flow rate of the target gas and balanced synthetic air was set to 1000 sccm and injected into the tube furnace. For the humid conditions, an appropriate amount of water vapor was mixed with formaldehyde to yield the desired gas concentration and relative humidity with a total flow rate of 1000 sccm. The electrical sensing resistance was recorded using a current source (Keithley 6220) and a nanovoltmeter (Keithley 2182) at a constant current of 10 nA with a time interval of 1 s under an LabView environment. The sensor response was defined to the resistance

relation using the following equation:

$$\text{Response(S)} = \frac{|R_a - R_g|}{R_g} = \frac{\Delta R}{R_g} \quad (1)$$

where R_a and R_g are the resistance in air and the target gas, respectively.

3. Results and discussion

An extremely effective formaldehyde gas sensor based on the SnO_2/NiO heterostructure was first investigated for the sensing characteristics. We obtained a record value in the sensing response toward formaldehyde gas detection with a low concentration of 10 ppm. As references, we tested pure SnO_2 or pure NiO-based sensor devices and they were compared with the SnO_2/NiO system. In the SnO_2/NiO heterostructures, the best performance was observed in the molar ratio of NiO 2 mM, which will be matched and discussed with the morphological effects and chemical states in the later sections. To emphasize the record score of the sensing property, we first discussed the sensing performances. We monitored the resistance dynamics in the pure SnO_2-based chemiresistive sensor depending on the operating temperature (a range of 200 °C to 500 °C) (Fig. 1a). Up to 350 °C, the initial resistance level in air (R_a) boosted as an increase of temperature. It is mainly contributed by the adsorption of oxygen molecules on the surface of the SnO_2 crystals that brings out an increase in the space-charge depletion layer with a large number of trapped free electrons on the surface [10,18]. When the temperature increased (400 – 500 °C), the R_a trend gradually reduced, which indicates that the electric potential for free carriers decreased [19] and its effect (intrinsic semiconductor property) is larger than the R_a variation by the adsorbed oxygen species. In the pure NiO (Fig. 1b) and SnO_2/NiO heterostructure (Fig. 1c)-based chemiresistive sensors, the NiO device showed a p-type oxide semiconductor behavior (oxidative gas interaction) and the SnO_2/NiO device exhibited an n-type semiconductor characteristic (reducing gas interaction) [3,9,20]. Unlike the pure SnO_2 device, both sensors showed operating temperature-dependent resistance trends based on the intrinsic semiconductor property of the potential barrier of electrical carriers; the R_a variations were sequentially reduced as a function of temperature (Fig. S2). Based on the results, we estimated the ppb formaldehyde/°C values as 31.738, 0.3195, and 139.981 for the pure SnO_2, pure NiO, and SnO_2/NiO (2 mM) heterostructured sensor, respectively. For the gas-in resistance level (R_g) i.e., formaldehyde interaction state, both sensors also appeared a gradual resistance variation with an operating temperature dependency. When the resistance trends were converted to the response dynamics based on the above-mentioned response Eq. (1) [20,21], we found an extreme sensing response result in the SnO_2/NiO (2 mM) heterostructure-based sensor device (Fig. S3). The summarized response trends as a function of operating temperature were shown in Fig. 1d. The pure SnO_2 and pure NiO chemiresistive devices showed the highest response value of 3161.41 and 396.15 at 300 °C, respectively, whereas the SnO_2/NiO (2 mM) blend structure showed a maximum value of 9121.74 at a lower temperature of 250 °C. It is a surprising result, in particular at the 10 ppm concentration and obviously a record result in both communities of formaldehyde gas sensors and SnOx-based sensor devices.

The transient response time (τ_{res}) that is defined as the time to reach 90% of the R_g level describes instant formaldehyde detection in the SnO_2/NiO heterostructure-based sensor [22]. The τ_{res} was 2.92 s in the SnO_2/NiO (2 mM) device, whereas that of pure SnO_2 was 1.95 s. The shorter τ_{res} was observed in the pure SnO_2 system, however, because of the extremely high response value of over 9000 in the SnO_2/NiO heterostructure, the slightly longer τ_{res} was observed. The chemiresistive gas sensor with formaldehyde interaction within 3 s is a considerably worthy device in the current state of formaldehyde gas detection.

Fig. 1f exhibits the sensitivity as the SnO_2/NiO (2 mM) heterostructure-based device is sequentially exposed to formaldehyde at various gas concentrations ranging from 0.01 ppm to 10 ppm at the optimized operating temperature of 250 °C. The sensitivity was monitored as the resistance variation with gas-in and -out reactions at each concentration (Fig. S4), and concentration-dependent response values revealed an exponential correlation with a coefficient of $R^2 = 0.9852$. In general, the sensitivity was evaluated by a linear relation in the concentration dependence [22,23]. However, the SnO_2/NiO (2 mM) heterostructure-based sensor showed an exponential relation, which is

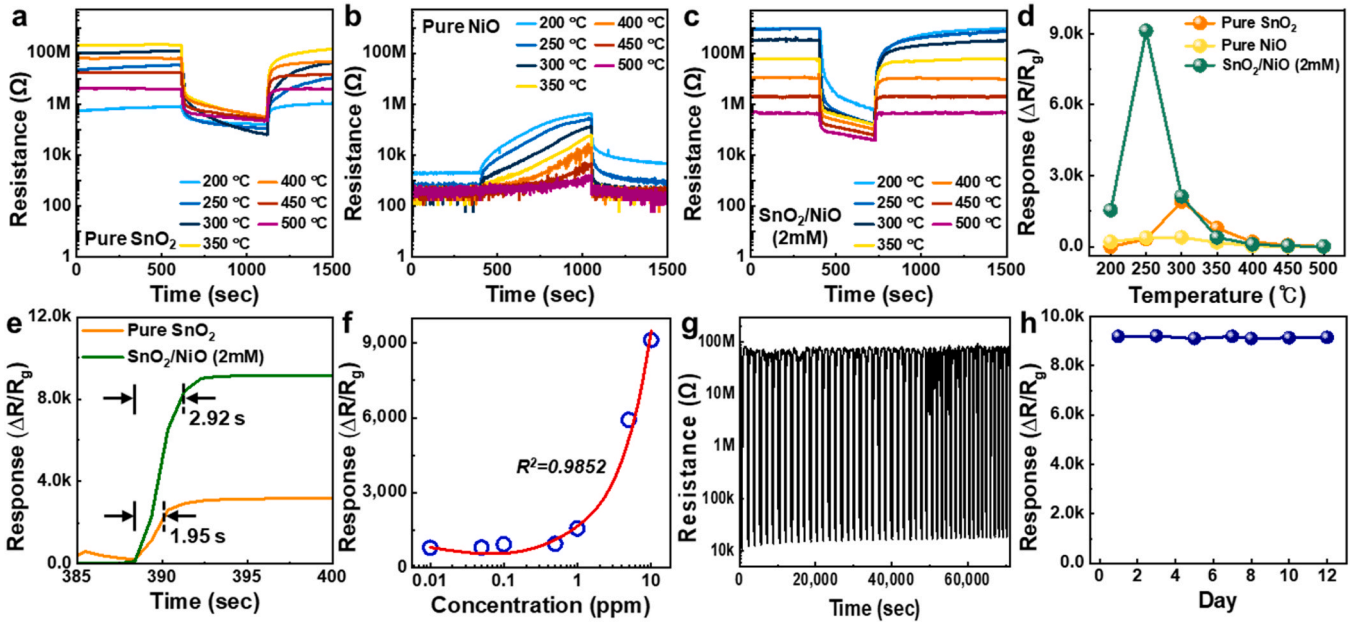

Fig. 1. Gas-sensing performances of SnO_2/NiO heterostructure-based chemiresistive device. A highlighted sensor is the SnO_2/NiO (2 mM) device: Temperature-dependent resistance dynamics of (a) pure SnO_2, (b) pure NiO, and (c) SnO_2/NiO heterostructure sensors. (d) Corresponding temperature-dependent response trends. (e) Transient response time for the pure SnO_2 and SnO_2/NiO heterostructure. (f) Sensitivity test depending on the formaldehyde concentration. (g) Repeated sensing transients (50 cycles) and (h) long-term reliability for 12 days in the detection of formaldehyde 10 ppm at 250 °C.

due to the dramatically superior response values after the 5 ppm concentration. Most of all, the World Health Organization (WHO) and the National Institute for Occupational Safety and Health (NIOSH) decided the safe exposure limit of formaldehyde to 0.08 ppm and 1 ppm, respectively [24]. They warn the workplace exposure limit that the legal airborne permissible exposure limit (PEL) is 0.75 ppm averaged over an 8-hour work shift [25]. It means that 1) the development of formaldehyde gas sensors is a crucial task and 2) the SnO_2/NiO chemiresistive device is a considerably powerful sensor because it showed response values of 791.20 and 1550.85 at the formaldehyde 0.05 ppm and 1 ppm, respectively.

The repeatability including the reproducibility of the SnO_2/NiO (2 mM) heterostructure-sensor device was investigated to confirm the preservation of the excellent response over a long period and a switching effect by the gas-in and -out cycles (Fig. 1g, highlighted 5 cycles were shown in Fig. S5a). For the cycle test, At ON part for the gas-in state, the formaldehyde 10 ppm was injected into the tube furnace, and in the OFF cycle (gas-out state), the target gas was pumped out and the furnace was cleaned to the synthetic air to ready for the next ON cycle. During the 50 cycles, the difference in the ON-OFF levels between the initial and final cycles was only 2.46%, demonstrating that the SnO_2/NiO (2 mM) device can be operated without the loss of sensing properties [26]. For the long-term stability, the SnO_2/NiO (2 mM) sensor was tested for 12 days (Fig. S5b), and the sensing responses were kept with over 9100 values (Fig. 1h) including a stable trend of the R_a variation (Fig. S5c).

The effect of humidity on the sensing response of the SnO_2/NiO (2 mM) chemiresistor was conducted under water vapor conditions from 0 to 80% RH (relative humidity). The resistance cycle and corresponding resistance variation are shown in Fig. S6a-b. From the response result (Fig. S6c), we find that the SnO_2/NiO (2 mM) sensor has an excellent sensing performance in humid harsh conditions up to 60% RH (the response loss was less than 12%) (Fig. S6d).

Selectivity is one of the most crucial factors in sensing properties to determine the effective gas sensor. Most of all, at a low concentration of 10 ppm, the selectivity in the detection of formaldehyde is considerably meaningful in an interior of toxic gas mixtures. We screened the sensing responses of other 9 test gases including acetone, CO, isoprene, ethyl benzene, xylene, H_2, CH_4, CO_2, and NO_2 and quantified their values with that of formaldehyde (all gases were at a concentration of 10 ppm and the operating temperature was 250 °C) (Fig. 2a). For the acetone and CO detection, the response value was approximately 50 (acetone = 49.2 and CO = 45.9), however in the other target gases, the values represented the ground levels less than 10 (inset figure). The overwhelming level of the formaldehyde response, 9121.74, leads to an ultra-exclusive selectivity, which is visualized in the radar map of Fig. 2b. We understand one of the reasons why the formaldehyde sensing reaction is extremely higher than other gas molecules in the chemical structure of dipole moment (D) [27]. Formaldehyde has a 2.3 D value, whereas other test

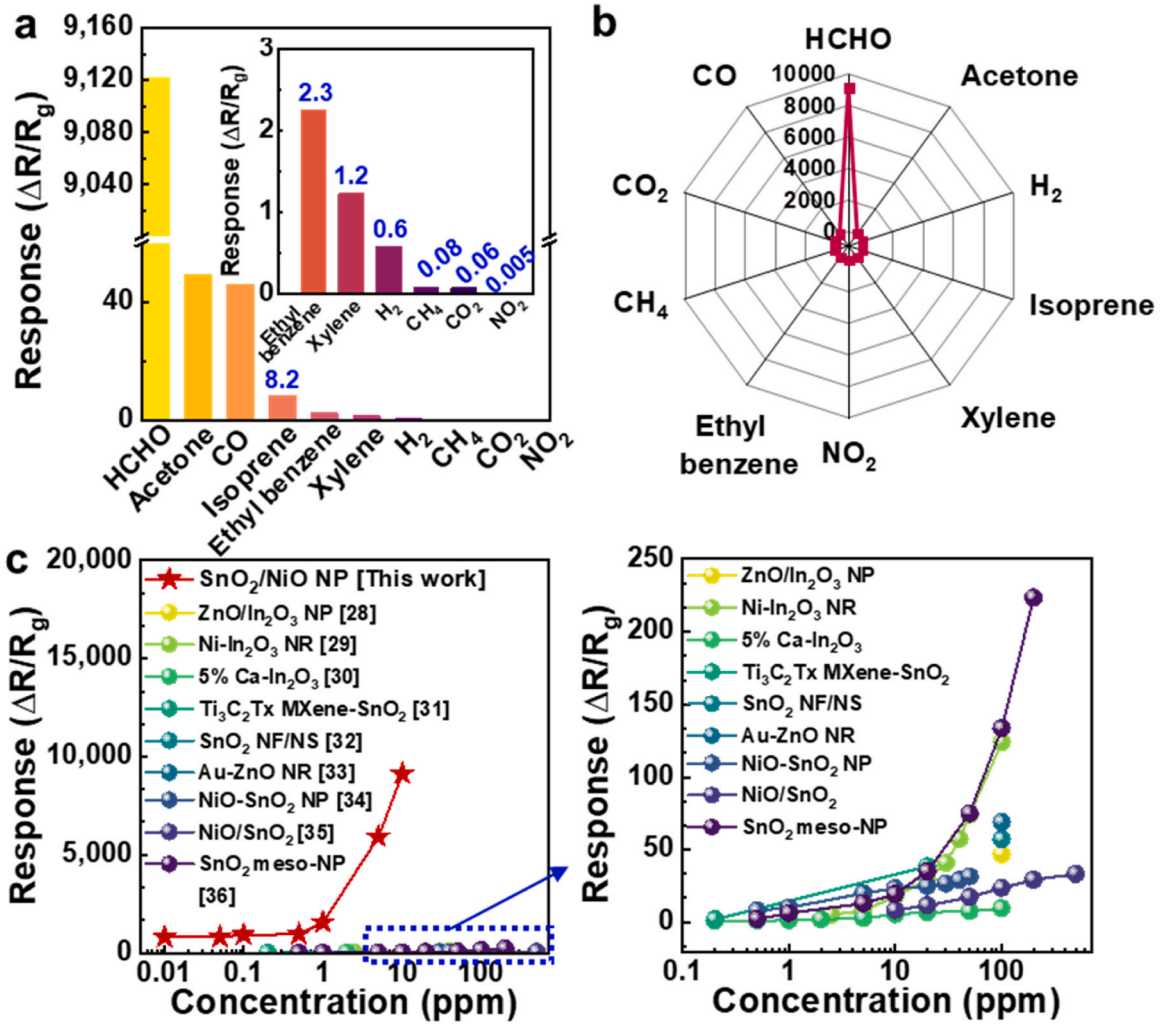

Fig. 2. (a) Ultra-exclusive selectivity in the detection of formaldehyde target gas (all test gases were 10 ppm concentration and the operating temperature was 250 °C for all gas sensors). (b) A radar map that represents Fig. 2a. (c) Comparison of sensing responses with previously reported formaldehyde gas sensors in various concentrations of formaldehyde (NP: nanoparticle, NR: nanorod, NF: nanofiber, and NS: nanosheet).

gases show values of 2.69 D for acetone, 0.122 D for CO, 0.29 D for isoprene, 0.58 D for ethylbenzene, 0.8 D for xylene, 0 D for H_2, CH_4, and CO_2, and 0.63 D for NO_2. Although the D values for formaldehyde and acetone are similar, the molecular size of formaldehyde is much smaller. As a result, formaldehyde gas molecules can effectively interact with oxygen species on the SnO_2/NiO (2 mM) heterostructure.

In comparison with the previously reported results toward formaldehyde detection, the SnO_2/NiO (2 mM) heterostructure-based sensor showed an extreme value in the sensing response, in particular over 1 ppm concentrations (Fig. 2c) [28–36].

To find reasons for the extremely high response in the SnO_2/NiO (2 mM) heterostructure-based sensor, we investigated external and internal morphologies of the SnO_2/NiO blend structures. In the sensing performances, the response value of 9121.74 was revealed in the NiO molar ratio of 2 mM. At the NiO conditions of 1 mM and 2.5 mM, the blend morphologies (SnO_2 = 2.5 mM) were evaluated for comparison. Fig. 3a displays SEM images positioned at three different magnifications. In the NiO 1 mM condition, SnO_2/NiO (1 mM), ca. 270 - 300 nm-sized particles were combined, and a random structured aggregation with ca. 1–2 μm in size was created (first row). When the NiO molar ratio increased to 2 mM, the random aggregation with a bright feature disappeared, and a well-blended morphology without prominent structures was observed (SnO_2/NiO (2 mM), second row). The 2.5 mM NiO condition provided further larger aggregation with ca. 5 μm sized structures (SnO_2/NiO (2.5 mM), third row). Depending on the NiO molar ratio, the SnO_2/NiO hetero-morphology was changed. We briefly understand that a more interconnected morphology without prominent aggregation allows effective chemical interaction with formaldehyde molecules, leading to an extreme sensing response.

We separately examined pure NiO morphologies as a function of molar ratio (0.5, 1, 2, and 5 mM) to find the dominant factor in the SnO_2/NiO interconnected morphology. In an overall view of SEM images (Fig. S7), the aggregated feature with a random structure gradually diminished up to the 2 mM condition; over 5 μm for the NiO 0.5 mM, ca. 1 μm for the NiO 1 mM, and ca. 500–600 nm for the NiO 2 mM. Upon the NiO molar concentration to 5 mM, a huge aggregation with ca. 200 nm-sized particles was revealed. For the NiO 2 mM condition, the most spread morphology with small particles (ca. 80 – 100 nm) and uniformly created formation (the morphologies that were detected at three different positions are similar – left, middle, and right images) were observed. We suggest that the most spread feature of NiO molecules without micron-sized aggregation might have a more blended structure with SnO_2. From the same perspective, we imagine that the morphology of the SnO_2/NiO heterostructure at the 2.5 mM/2 mM blend condition might be the most spread feature with a well-blended structure. Fig. S8 exhibited the SnO_2/NiO heterostructure morphologies depending on the blend ratios (the basis of NiO molar concentration was set to 2 mM and SnO_2 was controlled to 1.67, 2.5, 5, and 10 mM). Indeed, in the 2.5 mM/2 mM of SnO_2/NiO blend condition (second row), the most spread morphology, well-blended structure, and non-prominent aggregation were observed. In other blend ratios (1.67/2, 5/2, and 10/2 mM molar ratios), noticeable aggregation with hundreds to micron-sized particle structures was revealed.

In the internal morphology, the SnO_2/NiO heterostructures showed a network morphology that ca. 15 nm-sized particles are connected (Fig. 3b, HR-TEM). Importantly, the internal structures have an independence of NiO molar ratios (first column); all morphologies showed the particle-connected network structure. The particles were composed of SnO_2 and NiO domains, which is confirmed by the evaluation of interplanar spacing for the lattice fringes from the SnO_2 and NiO crystals (second column). The distances of primary lattice fringes were calculated to be 0.14 nm, 0.22 nm, 0.26 nm, and 0.33 nm, corresponding to the (211) of SnO_2, (200) of NiO, and (101), (110) planes of SnO_2, respectively [37,38]. The fast Fourier transform (FFT) patterns support the SnO_2 and NiO blend structures, as shown in the third column-positioned figures.

For the lattice information of SnO_2 and NiO crystal domains, XRD results provide crystal structures in detail. All diffraction profiles of the SnO_2/NiO heterostructures as a function of NiO molar ratio to 1, 2, and 2.5 mM indicated the blended crystal structure of SnO_2 and NiO phases (Fig. 4a), which is consistent with the TEM results. All Bragg reflections were well-indexed to the rutile structure of SnO_2 (pink circle, ICDD card No. 01–070-6995) [3,39] and NiO crystal phase (blue circle, ICDD card No. 03–065-6920) [40]. The predominant Bragg peaks at two-theta of 26.62°, 33.86°, and 51.78° are indexed as (110), (101), and (211) planes for the SnO_2, respectively, and at two-theta of 44.59° is indexed as (200) plane for the NiO. Compared to the XRD patterns of pure SnO_2 (yellowish graph in Fig. 4a) and pure NiO (Fig. S9a-b), the diffraction peaks showed considerably higher reflection intensities in the SnO_2/NiO heterostructures. In comparison with the SnO_2/NiO heterostructure systems, the reflection intensity exhibited NiO molar ratio-dependent crystallinity; it has a sequence order of SnO_2/NiO (2 mM), SnO_2/NiO (1 mM), and SnO_2/NiO (2.5 mM). A two-theta peak at 26.62° was highlighted to investigate the crystallinity and crystalline domain size in

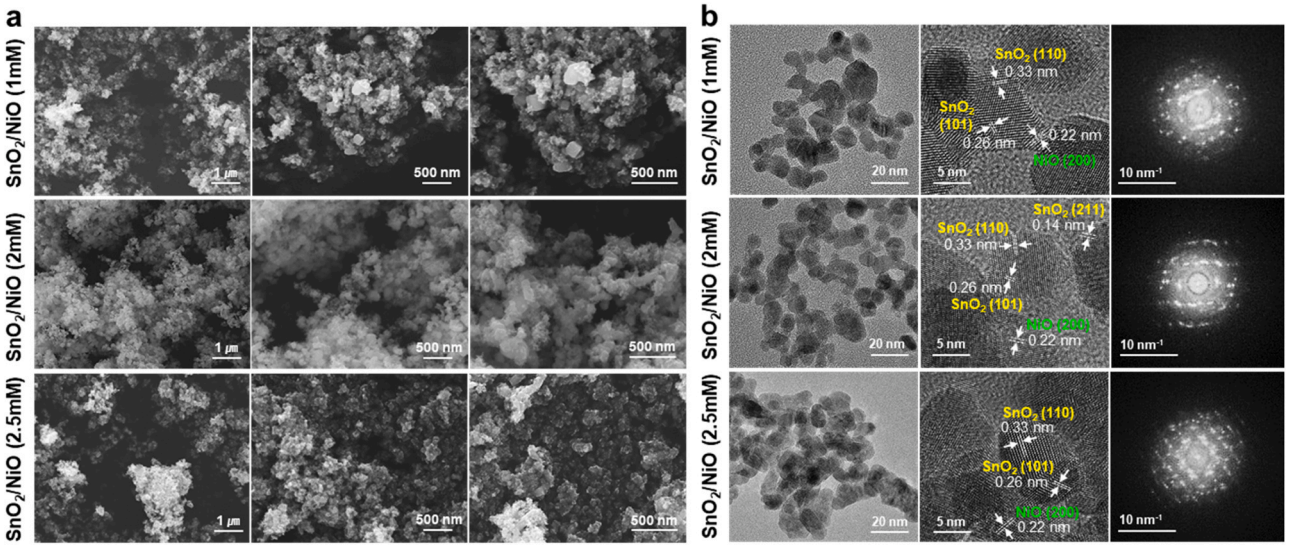

Fig. 3. External and internal morphological characterization of SnO_2/NiO heterostructures: (a) SEM images (X 15,000: left, X 30,000: middle, X 45,000: right column) and (b) HR-TEM images including FFT patterns (X 50 K: left, X 1 M: middle, FFT: right column).

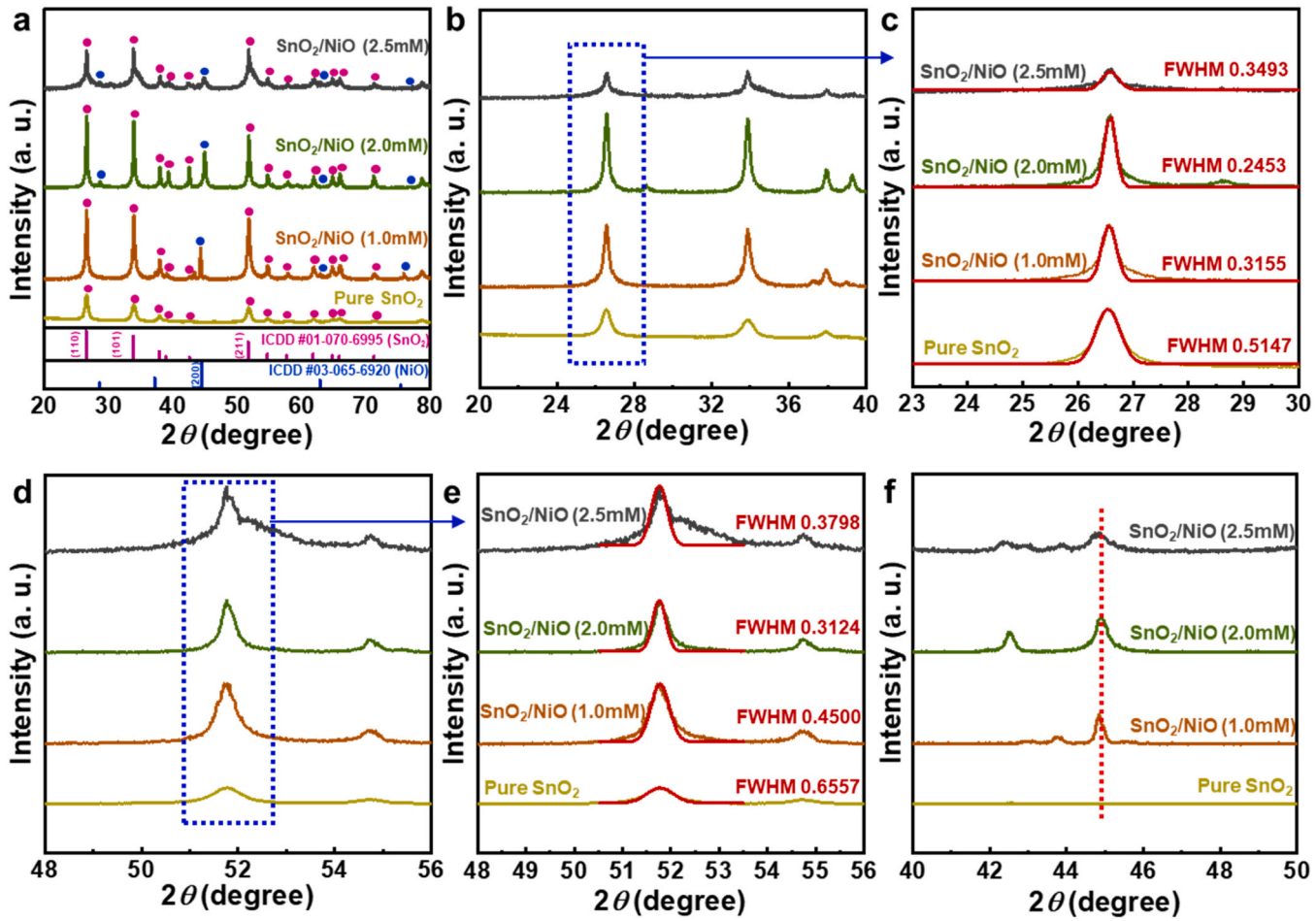

Fig. 4. Internal crystal structures of SnO_2/NiO heterostructures with a NiO molar ratio dependency: (a) XRD profiles with a full scan, (b) enlarged view of XRD patterns with a range of 20 – 40 degrees, (c) Gaussian fittings of diffraction curves in a range of 23 – 30 degrees, (d) focused view of XRD results with a range of 48 – 56 degrees, (e) corresponding Gaussian fitting curves at 51.78°, and (f) highlighted XRD profiles with a range of 40 – 50 degrees.

the (110) lattice plane of SnO_2 (Fig. 4b). The lattice phase was diffracted to the highest intensity in the SnO_2/NiO (2 mM), demonstrating that the SnO_2 crystal was generated with a high degree of crystallinity in the heterostructure. The crystallite size was calculated using the following equation, the Debye-Scherrer relation [41]:

$$\mathrm{D(crystallite\ size)} = \frac{k\lambda}{\beta\ \cos\theta}, \beta = \frac{\pi}{180} \times FWHM \quad (2)$$

where k is the Scherrer constant of 0.9, λ is the X-ray wavelength, β is the line broadening at half the maximum intensity (the full width at half maximum, FWHM) in radians. The FWHM values at the (110) peak of 26.6° were obtained from a Gaussian fitting (Fig. 4c), and the crystallite sizes of the SnO_2 crystal domains were calculated. The estimated sizes were 332.73 Å, 258.78 Å, 233.72 Å, and 158.60 Å for the SnO_2/NiO (2 mM), SnO_2/NiO (1 mM), SnO_2/NiO (2.5 mM), and pure SnO_2, respectively. Compared with pure SnO_2, the SnO_2 crystal size for the (110) phase was larger in the heterostructure, the NiO 2 mM approved the generation of the largest SnO_2 crystal phase along the (110) plane of the heterostructure. In the same manner, the crystallite sizes of the SnO_2 (211) phase were estimated at two-theta of 51.78° (Fig. 4d-e); 282.79 Å for the SnO_2/NiO (2 mM), 232.51 Å for the SnO_2/NiO (2.5 mM), 196.24 Å for the SnO_2/NiO (1 mM), and 134.68 Å for the pure SnO_2. For the NiO crystal domain, the main Bragg peak at 44.59 ° was the most highlighted in the SnO_2/NiO (2 mM) heterostructure (Fig. 4f and Fig. S9b). Consequently, from the morphology study, we summarize that the SnO_2/NiO heterostructure at the SnO_2 and NiO molar ratio to 2.5 mM and 2 mM, respectively, has an ideal morphology, well-blended external morphology, internally interconnected network that SnO_2 and NiO crystals were created by boosting their lattice structures with a high degree of crystallinity including large crystallite size. In other words, the SnO_2 and NiO crystal phases were generated where they have a synergetic effect in the creation of crystalline morphology. This heterostructural morphology leads to the record result in the sensing response of the formaldehyde detection.

To find the determination state of the synergetic crystalline morphology of the SnO_2/NiO heterostructure in the solution state, UV–visible absorption spectra were recorded at the liquid phase of the initial and final stages in the synthetic process. At the initial stage, where SnO_2 and NiO precursors were blended and dissolved in di-water, respectively, before 24 h mixing (Fig. 5a-e, first row), pure SnO_2 and pure NiO showed absorption spectra with two peaks at 264.0 nm and 330.1 nm for the SnO_2 (Figs. 5a) and 355.8 nm for the NiO (Fig. 5b), respectively [42]. When the SnO_2 and NiO blended, in particular at the NiO ratio of 2 mM condition (SnO_2/NiO (2 mM)), two absorption peaks that were observed at the pure SnO_2 solution were revealed with a shift of the absorption band (276.2 nm and 346.6 nm in Fig. 5d), whereas other blend conditions (SnO_2/NiO (1 mM) and SnO_2/NiO (2.5 mM), Figs. 5c and 5e) exhibited the broad bands without noticeable peaks. In the final synthesis stage of the liquid phase that the synthesized powders were dissolved in ethanol (Fig. 5f-j, second row), an absorption band of the SnO_2/NiO (2 mM) (Fig. 5i) showed a similar spectrum to the initial synthesis stage of the SnO_2/NiO (2 mM) with two red-shifted peaks at 297.3 nm and 357.2 nm. Other blend structures of the SnO_2/NiO (1 mM) (Fig. 5h) and SnO_2/NiO (2.5 mM) (Fig. 5j) followed the

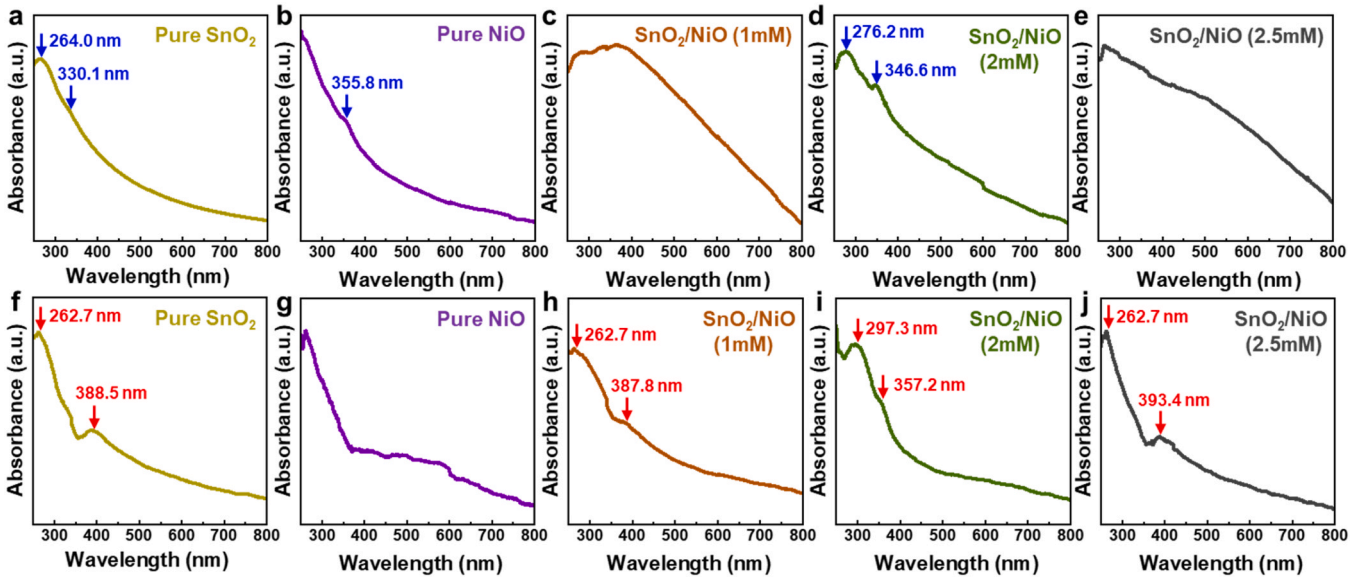

Fig. 5. UV–vis absorption spectra of pure SnO_2, pure NiO, SnO_2/NiO (1 mM), SnO_2/NiO (2 mM), and SnO_2/NiO (2.5 mM) in the solution state. The first row is the initial stage of the synthesis process (dispersion in di-water) and the second row is the final stage that the synthesized powders were dissolved in ethanol.

absorption spectrum of pure SnO_2 (Fig. 5f) with two absorption peaks at 262.7 nm and 388.5 nm. Fig. 5 results indicate that the crystalline domains of SnO_2 phases were dominantly generated at the initial solvated state, encouraging the formation of NiO crystal structures. The solvated crystalline structure was kept in the final solid state, which lead to the synergetic crystal morphology of the SnO_2/NiO heterostructure. It uniquely appears in the SnO_2/NiO heterostructure of the 2.5/2 mM molar ratio condition.

The FT-IR spectra of the SnO_2/NiO heterostructure chemically support the synergetic crystalline structure in the interconnected morphology (Fig. S10). With pure SnO_2, both spectra showed three potential peaks at 1633 cm^{-1}, 1461 cm^{-1}, and 1423 cm^{-1}, which are assigned to the H-O-H vibration [43], O-OH^- group [43], and O-H bending proving the existence of -COOH [44], respectively. In the pure SnO_2 sample, however, a strong absorption band in the range of 595–712 cm^{-1} including a strong peak at 630 cm^{-1} and an absorption potential at 571 cm^{-1} were revealed, they are attributed to the Sn-O and Sn-O-Sn vibration, respectively [45]. Compared to the pure SnO_2, the SnO_2/NiO heterostructure showed two broad absorption bands with ranges of 451–595 cm^{-1} and 595–735 cm^{-1} according to the SnO_2 and NiO interaction, respectively. In particular, three absorption potentials at 628 cm^{-1}, 510 cm^{-1}, and 451 cm^{-1} can be detected in the ranges, which are dedicated to the SnO-N [46], O-Sn-O [46], and Ni-O [47] stretching vibration, respectively. It describes that the SnO_2 and NiO crystal structures are formed in the interconnected morphology as they have chemical interactions.

As the other terms of chemical compositions to demonstrate the correlation between the heterostructural morphology and sensing response, XPS study was performed for the three SnO_2/NiO heterostructures. The XPS survey spectra indicate the heterostructures have Sn, O, and Ni elements on the surface (Fig. S11a) and high-resolution XPS results for the Sn 3d (Fig. S11b), O 1 s (Fig. S11c), Ni 2p (Fig. S11d) core levels, and deconvolution fittings (Fig. 6) provide detailed chemical states according to the SnO_2/NiO blend. For the Sn 3d state, all blend spectra showed a slight shift with 0.3 eV toward higher energy compared with the pure SnO_2 (Fig. S11b), which is attributed to the electron flow by SnO_2 and NiO chemical interaction [48]. When the spectra were deconvoluted (Fig. 6a – SnO_2/NiO (1 mM), 6d – SnO_2/NiO (2 mM), and 6 g – SnO_2/NiO (2.5 mM)), the Sn $3d_{3/2}$ and Sn $3d_{5/2}$ peaks were detected at ca. 493.6 eV and 485.2 eV, respectively. Each peak was split into two peaks for Sn^{4+} and ligand-type bonding of Sn atoms (Sn-L, Sn^0) [49]; ca. 493.49 eV and 491. 76 eV for the Sn $3d_{3/2}$ and ca. 485.07 eV and 483.06 eV for the Sn $3d_{5/2}$ spin-orbit peak.

The detection of Sn^{4+} species indicates the presence of oxygen vacancies in the SnO_2/NiO heterostructure, the O 1 s core level spectra demonstrate it in detail. All three spectra were deconvoluted into three peaks at ca. 530.5 eV, ca. 531.4 eV, and ca. 532.4 eV corresponding to O_{lat} (lattice oxygen species), O_{vac} (oxygen vacancies), and O_{ads} (chemisorbed oxygen species) (Fig. 6b, e, and h). The O_{lat} is ascribed to the lattice oxygen of the SnO_2/NiO heterostructure and involves interactions between the O-Sn and O-Ni [50]. The O_{vac} is related to non-stoichiometric oxygen that dominates oxygen-deficient regions as oxygen vacancies [51], which significantly influences the sensing properties because it enhances the chemical interaction between the adsorbed oxygen molecules and the target gas. The percentage fractions of O_{vac} area were estimated to be 16.42% for the SnO_2/NiO (1 mM) (Figs. 6b), 22.76% for the SnO_2/NiO (2 mM) (Figs. 6e), and 13.43% for the SnO_2/NiO (2.5 mM) (Fig. 6h). We thereby find one of the reasons why the SnO_2/NiO (2 mM) heterostructure showed the overwhelming sensing response. In the Ni 2p core level, all heterostructures showed a spin-orbit splitting of Ni $2p_{1/2}$ and Ni $2p_{3/2}$ state, each state was deconvoluted into three peaks in the range of ca. 848.6 – 864.9 eV (Ni $2p_{3/2}$) and in the range of ca. 868.7 – 887 eV (Ni $2p_{1/2}$ state) (Fig. 6c, f, and i) [37,52]. It implies the existence of Ni^{2+} species on the surface of the SnO_2/NiO heterostructure.

Chemically interconnected SnO_2/NiO morphology generates the formation of a p-n junction between p-type NiO and n-type SnO_2 crystal domains, which facilitates the modulation of electronic band structure in the heterostructure. Fig. 7a-c displays tauc plots for pure SnO_2, pure NiO, and SnO_2/NiO (2 mM) that were derived by the following equation based on the UV–vis absorption spectra:

$$(\alpha h\nu)^{\gamma} = A(h\nu - E_g) \tag{3}$$

where α is the absorption coefficient, h is the Plancks constant, ν is the light frequency, A is a proportionality constant that depends on the electron-hole mobility, γ is 1/2 or 2 value for indirect or direct band gap, respectively, and E_g is the band gap [53]. The direct E_gs were extrapolated to be 3.58 eV for pure SnO_2, 3.64 eV for pure NiO, and 3.52 eV for the SnO_2/NiO (2 mM) heterostructure, which describes that the SnO_2/NiO heterostructure has an intermediate electronic structure. With the E_g value, electron transfer behavior was evaluated from the work function (Φ_F) and valence band level. Fig. 7d shows UPS energy

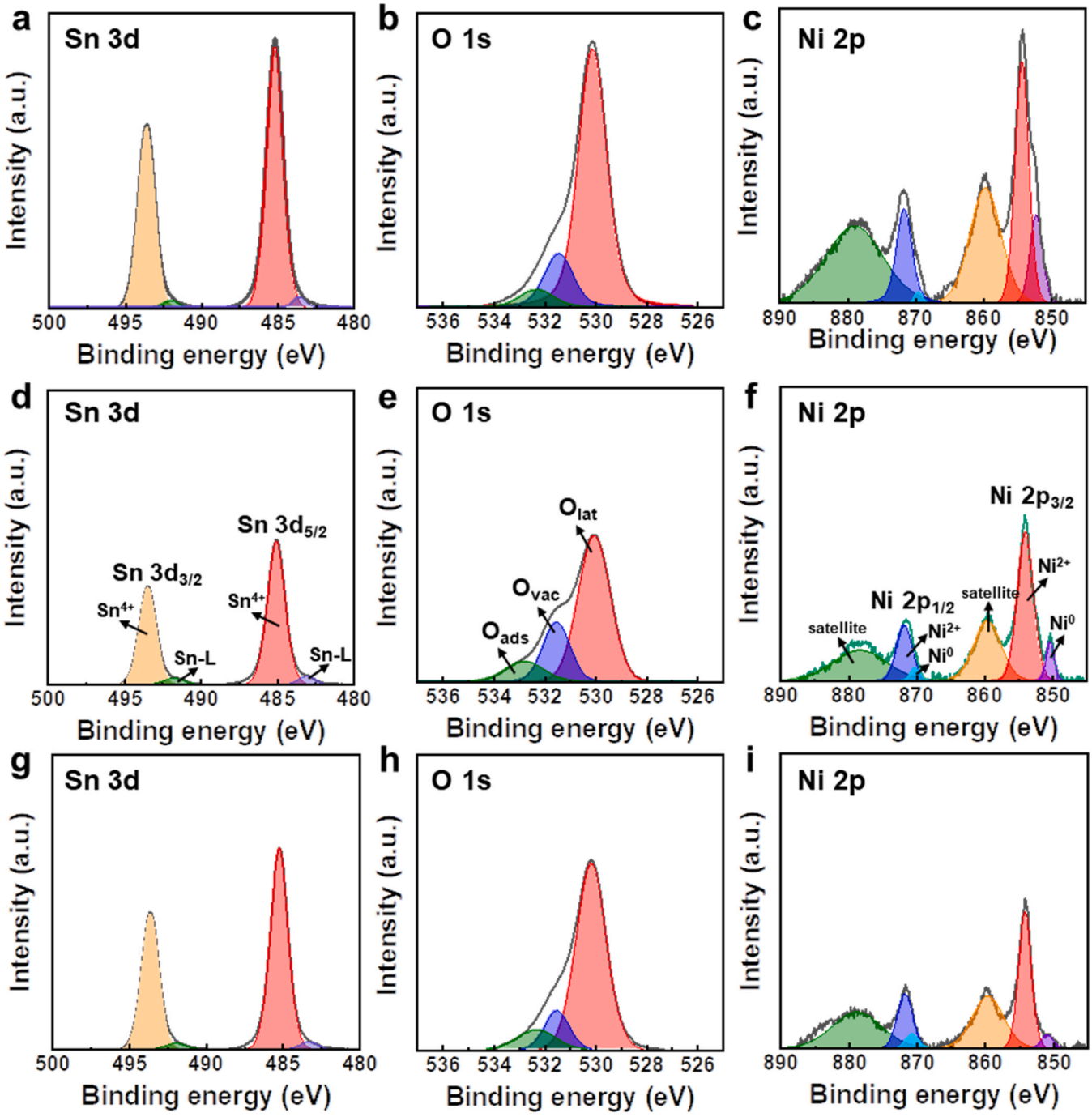

Fig. 6. Chemical states of the surface of the SnO_2/NiO heterostructures: High-resolution XPS spectra of Sn 3d, O 1 s, and Ni 2p core levels. The first row (a-c) is for the SnO_2/NiO (1 mM), the second row (d-f) is for the SnO_2/NiO (2 mM), and the third row (g-i) is for the SnO_2/NiO (2.5 mM).

distribution spectra including both the secondary electron cut-off (Fig. 7e, left-side figure) and the valence band edge (Fig. 7e, right-side figure) regions. The Φ_F of a metal oxide surface is given by the following equation:

$$\Phi_F = h\nu - E_{sc} \quad (4)$$

where the $h\nu$ term is the photon energy of the incident He(I) line of a He discharge lamp and E_{sc} is the secondary cut-off energy, and is obtained from the fitting line between the cut-off edge and the baseline [54]. The maximum energy of the valence band from the Fermi level can be estimated to the linear portion of the low binding energy side of the valence band peak to the energy axis [54,55]. Based on the two concepts, the Φ_Fs and the maximum energies of the valence bands were calculated for the three systems, and the energy level diagrams were suggested as shown in Fig. 7f. We find that both Φ_F and valence band level are placed at the intermediate position in the SnO_2/NiO (2 mM) heterostructure, indicating a result of the bend banding by the formation of the p-n heterojunction of SnO_2 and NiO.

4. Conclusions

In this work, we achieved a record value of sensing response with a 9121.74 in the SnO_2/NiO heterostructure sensor device toward formaldehyde detection at a 10 ppm concentration. With the extremely high

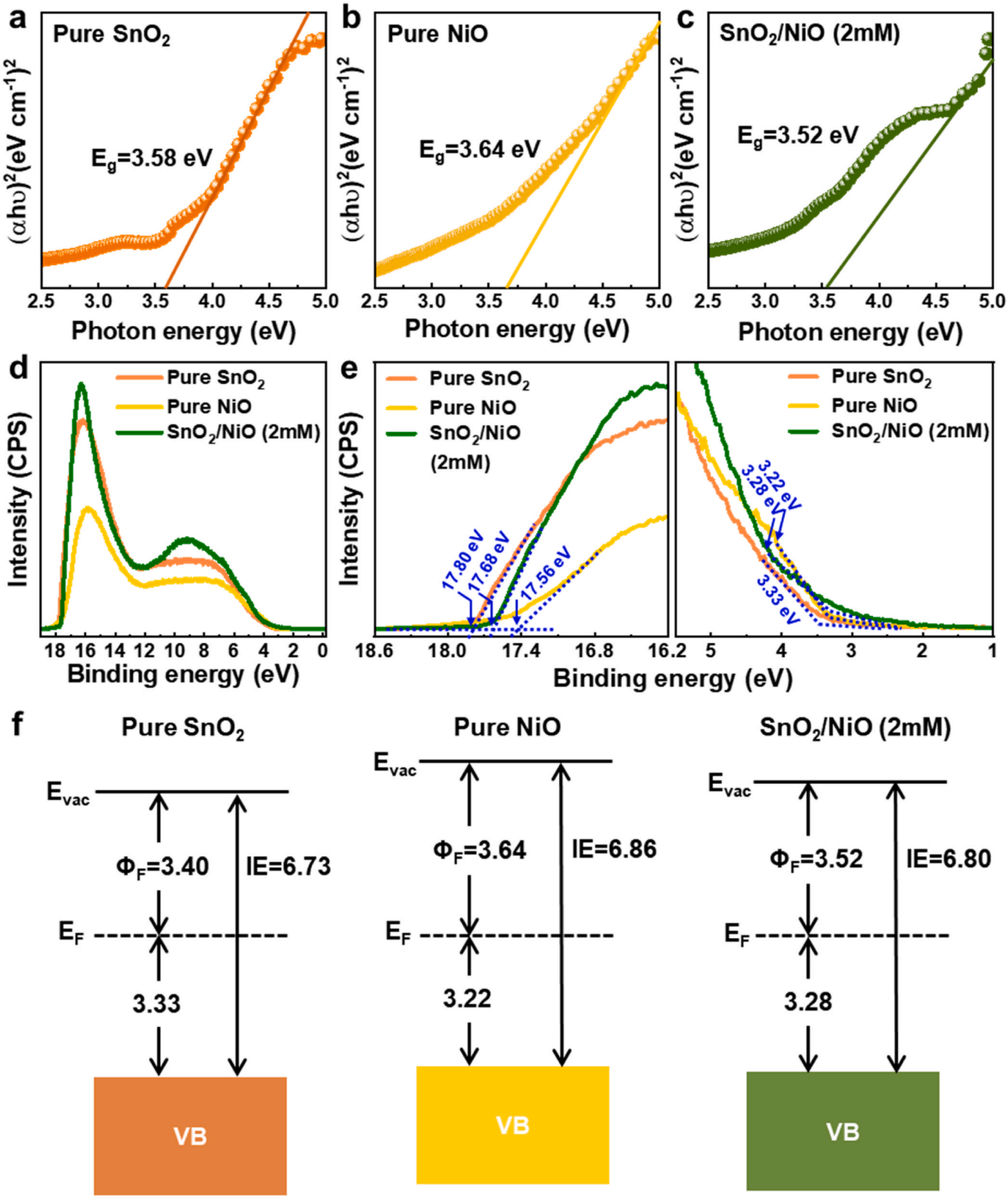

Fig. 7. Determination of electronic structure for pure SnO2, pure NiO, and SnO_2/NiO heterostructure: Tauc plots for direct band gap UPS curves in the secondary cut-off and the valence band region.

response, the heterostructure chemiresistive sensor showed a transient response time within 3 s and a significant stable result in repeatability including reproducibility with ca. 2% loss in the gas ON-OFF level in the 50 cycles and 12 days. The overwhelming sensing response highlights the ultra-exclusive selectivity in formaldehyde sensing, which becomes a front-runner chemiresistive device in the research community of formaldehyde sensors. The SnO_2 and NiO of 2.5 mM and 2 mM blend molar ratio under a facile one-step mixing process allows an interconnected

morphology that is comprised of SnO_2 and NiO nanoparticles. They were created in the morphology by encouraging the formation of crystal phases each other, and thus the crystal phases showed a high degree of crystallinity and large crystallite size. The synergetic crystal phases of SnO_2/NiO heterostructure in the interconnected morphology were chemically constructed, facilitating effective chemical communication with formaldehyde gas molecules in terms of not only surface and internal crystal structure but also electronic band structure. We believe that our work will bring a ripple effect based on a huge potential and will become a sensation model in the SnO_2/NiO heterostructure-based formaldehyde sensor field.

CRediT authorship contribution statement

Kim Yu Jin: Writing – review & editing, Writing – original draft, Supervision, Investigation, Data curation, Conceptualization. **Lee Jihyun:** Methodology, Formal analysis, Conceptualization. **Lee Wooyoung:** Supervision, Resources, Project administration, Funding acquisition.

Declaration of Competing Interest

All authors declare that they have no known competing financial interests or personal relationships that could have appeared to influence the work reported in this paper.

Data availability

Data will be made available on request.

Acknowledgments

This work was supported by the Technology Innovation Program (‘20013621′, Center for Super Critical Material Industrial Technology) funded by the Ministry of Trade, Industry & Energy (MOTIE, Korea). This research was supported by the National Research Foundation of Korea (NRF) grant funded by the Korea government (MIST) (NRF-2022M3H4A3053304, National Core Materials Research Center (Platform type)). This research was also supported by the Basic Science Research Program and the Korea Initiative for fostering University of Research and Innovation (KIURI) Program through the National Research Foundation of Korea (NRF) funded by the Ministry of Education (NRF-2019R1A6A1A11055660) and the Korean government (MSIT) (NRF-2020M3H1A1077207).

Appendix A. Supporting information

Supplementary data associated with this article can be found in the online version at doi:10.1016/j.snb.2023.135257.

References

[1] X. Kang, N. Deng, Z. Yan, Y. Pan, W. Sun, Y. Zhang, Resistive-type VOCs and pollution gases sensor based on SnO_2: a review, Mater. Sci. Semicond. 138 (2022) 106246.
[2] Y. Masuda, Recent advances in SnO_2 nanostructure based gas sensors, Sens. Actuators B: Chem. 364 (2022) 131876.
[3] S. Das, V. Jayaraman, SnO_2: a comprehensive review on structures and gas sensors, Prog. Mater. Sci. 66 (2014) 112.
[4] D. Manikandan, R. Murugan, Genesis and tuning of ferromagnetism in SnO_2 semiconductor nanostructures: comprehensive review on size, morphology, magnetic properties and DFT investigations, Prog. Mater. Sci. 130 (2022) 100970.
[5] Y. Liu, A. Yamaguchi, Y. Yang, A. Aismada, S. Uchida, H. Abe, S. Ueda, K. Yamaguchi, T. Tanabe, M. Miyauchi, Synthesis and characterization of the orthorhombic Sn_3O_4 polymorph, Angew. Chem. 62 (2023) e202300640.
[6] S. Amith, K. Gurunathan, Active sites tailored rGo-PPy nanosheets with high crystalline tetragonal SnO_2 nanocrystals for ammonia e-sensitization at room temperature, J. Alloy. Compd. 960 (2023) 170819.
[7] C. Li, P.G. Choi, Y. Masuda, Highly sensitive and selective gas sensors based on NiO/MnO_2@NiO nanosheets to detect allyl mercaptan gas released by humans under psychological stress, Adv. Sci. 9 (2022) 2202442.
[8] Q. Li, W. Zeng, Y. Li, Metal oxide gas sensors for detecting NO_2 in industrial exhaust gas: Recent developments, Sens. Actuators B: Chem. 359 (2022) 131579.
[9] T.P. Mokoena, H.C. Swart, D.E. Motaung, A review on recent progress of p-type nickel oxide based gas sensors: future perspective, J. Alloy. Compd. 805 (2019) 267.
[10] X. Ma, Z. Ying, F. Wen, L. Li, X. Zheng, P. Zheng, G. Wang, Gas-sensitive properties of ZnO/$ZnCo_2O_4$ made from sodium citrate against formaldehyde, J. Electron. Mater. 51 (2022) 7009.
[11] S. Das, S. Mojumder, D. Saha, M. Pal, Influence of major parameters on the sensing mechanism of semiconductor metal oxide based chemiresistive gas sensors: a review focused on personalized healthcare, Sens. Actuators B: Chem. 352 (2022) 131066.
[12] D. Meng, D. Liu, G. Wang, Y. Shen, X. San, M. Li, F. Meng, Low-temperature formaldehyde gas sensors based on NiO-SnO_2 heterojunction microflowers assembled by thin porous nanosheets, Sens. Actuators B: Chem. 273 (2018) 418.
[13] K. Zhuo, J. Wang, W. Hou, Y. Cheng, S. Sang, SnO_2 doped NiO heterostructure nanofibers prepared by electrostatic spinning: a novel sensor for catalytic oxidation of formaldehyde, Microchem. J. 180 (2022) 107579.
[14] S. Das, A. Kumar, J. Singh, M. Kumar, Fabrication and modeling of laser ablated NiO nanoparticles decorated SnO_2 based formaldehyde sensor, Sens. Actuators B: Chem. 387 (2023) 133824.
[15] V. Gerbreders, M. Krasovska, E. Sledevskis, A. Gerbreders, I. Mihailova, E. Tamanis, A. Ogurcovs, Hydrothermal synthesis of ZnO nanostructures with controllable morphology change, CrstEngComm 22 (2022) 1346.
[16] W. Bu, Y. Zhang, Q. Qin, Y. Li, X. Chuai, Z. Zhou, C. Hu, T. Wang, P. Sun, F. Liu, G. Lu, Improved ppb-level NO_2 conductometric sensor induced by trace Au on SnO_2 nanosheet, Sens. Actuators B: Chem. 379 (2023) 133237.
[17] J. Lee, H. Min, Y. Choe, Y. Lee, K. Kin, H. Lee, W. Lee, Highly sensitive and selective detection of benzene, toluene, xylene, and formaldehyde using Au-coated SnO_2 nanorod arrays for indoor air quality monitoring, Sens. Actuators B: Chem. 394 (2023) 134359.
[18] Y. Kong, Y. Li, X. Cui, L. Su, D. Man, T. Lai, L. Yao, X. Xiao, Y. Wang, SnO_2 nanostructured materials used as gas sensors for the detection of hazardous and flammable gases: a review, Nano Mater. Sci. 4 (2022) 339.
[19] P. Salev, L. Fratino, D. Sasaki, R. Berkoun, J. Valle, Y. Kalcheim, Y. Takamura, M. Rozenberg, I. Schuller, Transverse barrier formation by electrical triggering of a metal-to-insulator transition, Nat. Commun. 12 (2021) 5499.
[20] J. Walker, P. Karnati, S. Akbar, P. Morris, Selectivity mechanisms in resistive-type metal oxide heterostructural gas sensors, Sens. Actuators B: Chem. 355 (2022) 131242.
[21] A. Staerz, U. Weimar, N. Barsan, Current state of knowledge on the metal oxide based gas sensing mechanism, Sens. Actuators B: Chem. 358 (2022) 131531.
[22] C. Yuan, J. Ma, Y. Zou, G. Li, H. Xu, V. Sysoev, X. Cheng, Y. Deng, Modeling interfacial interaction between gas molecules and semiconductor metal oxides: A new view angle on gas sensing, Adv. Sci. 9 (2022) 2203594.
[23] B. Mondal, P. Gogoi, Nanoscale heterostructured materials based on metal oxides for a chemiresistive gas sensor, ACS Appl. Electron. Mater. 4 (2022) 59.
[24] L. Zhu, J. Wang, J. Liu, Z. Xu, M.S. Nasir, X. Chen, Z. Wang, S. Sun, Q. Ma, J. Liu, J. Feng, J. Liang, W. Yan, In situ enrichment amplification strategy enabling highly sensitive formaldehyde gas sensor, Sens. Actuators B: Chem. 354 (2022) 131206.
[25] L. Zhang, Formaldehyde: Exposure, Toxicity and Health Effects, UK, 2018.
[26] S. Gasso, M. Sohal, A. Mahajan, MXene modulated SnO_2 gas sensor for ultra-responsive room-temperature detection of NO_2, Sens. Actuators B: Chem. 357 (2022) 131427.
[27] Z. Wang, M. Guo, X. Mu, S. Sen, T. Insley, A.J. Mason, P. Kral, X. Zeng, Highly sensitive capacitive gas sensing at ionic liquid-electrode interfaces, Anal. Chem. 88 (2016) 1959.
[28] L. Ma, H. Fan, H. Tian, J. Fang, X. Qian, The n-ZnO/n-In_2O_3 heterojunction formed by a surface-modification and their potential barrier-control in methanal gas sensing, Sens. Actuators B: Chem. 222 (2016) 508.
[29] X. Zhang, D. Song, Q. Liu, R. Chen, J. Hou, J. Liu, H. Zhang, J. Yu, P. Liu, J. Wang, Designed synthesis of Ag-functionalized Ni-doped In_2O_3 nanorods with enhanced formaldehyde gas sensing properties, J. Mater. Chem. C. 7 (2019) 7219.
[30] Q. Liang, X. Zou, H. Chen, M. Fan, G. Li, High-performance formaldehyde sensing realized by alkaline-earth metals doped In_2O_3 nanotubes with optimized surface properties, Sens. Actuators B: Chem. 304 (2020) 127241.
[31] G. Niu, M. Zhang, B. Wu, Y. Zhuang, R. Ramachandran, C. Zhao, F. Wang, Nanocomposites of pre-oxidized Ti3C2Tx MXene and SnO_2 nanosheets for highly sensitive and stable formaldehyde gas sensor, Ceram. Int. 49 (2023) 2583.
[32] D. Wang, K. Wan, M. Zhang, H. Li, P. Wang, X. Wang, J. Yang, Constructing hierarchical SnO_2 nanofiber/nanosheets for efficient formaldehyde detection, Sens. Actuators B: Chem. 283 (2019) 714.
[33] J. Huang, H. Liang, J. Ye, D. Jiang, Y. Sun, X. Li, Y. Geng, J. Wang, Z. Qian, Y. Du, Ultrasensitive formaldehyde gas sensor based on Au-loaded ZnO nanorod arrays at low temperature, Sens. Actuators B: Chem. 346 (2021) 130568.
[34] S. Das, A. Kumar, J. Singh, M. Kumar, Fabrication and modeling of laser ablated NiO nanoparticles decorated SnO_2 based formaldehyde sensor, Sens. Actuators B: Chem. 387 (2023) 133824.
[35] S. Din, M. Haq, M. Sajid, R. Khatoon, X. Chen, L. Li, M. Zhang, L. Zhu, Development of high-performance sensor based on NiO/SnO_2 heterostructures to study sensing properties towards various reducing gases, Nanotechnology 31 (2020) 395502.

[36] P. Liu, J. Wang, H. Jin, M. Ge, F. Zhang, C. Wang, Y. Sun, N. Dai, SnO_2 mesoporous nanoparticle-based gas sensor for highly sensitive and low concentration formaldehyde detection, RSC Adv. 13 (2023) 2256.
[37] S. Bai, J. Liu, J. Guo, R. Luo, D. Li, Y. Song, C.C. Liu, A. Chen, Facile preparation of SnO_2/NiO composites and enhancement of sensing performance to NO_2, Sens. Actuators B: Chem. 249 (2017) 22.
[38] T. Liu, Z. Yu, Y. Liu, J. Gao, X. Wang, H. Suo, X. Yang, C. Zhao, F. Liu, Gas sensor basd on Ni foam: SnO_2-decorated NiO for toluene detection, Sens. Actuators B: Chem. 318 (2020) 128167.
[39] T. Onishi, M. Fujishima, H. Tada, Solar-driven one-compartment hydrogen peroxide-photofuel cell using bismuth vanadate photoanode, ACS Omega 3 (2018) 12099.
[40] S.D. Dhas, P.S. Maldar, M.D. Patil, A.B. Nagare, M.R. Waikar, R.G. Sonkawade, A. V. Moholkar, Synthesis of NiO nanoparticles for supercapacitor application as an efficient electrode material, Vacuum 181 (2020) 109646.
[41] S. Wang, R. Pang, T. Tan, H. Wu, Q. Wang, C. Li, S. Zhang, T. Tan, H. You, H. Zhang, Achieving high quantum efficiency broadband NIR $Mg_4Ta_2O_9$:Cr^{3+} phosphor through lithium-ion compensation, Adv. Mater. 35 (2023) 2300124.
[42] M. Homocianu, A. Airinei, A.M. Ipate, P.P. Dorneanu, C. Hamciuc, Optical properties of some fluorinated poly(1,3,4-oxadiazole-ether)s in homogeneous and heterogeneous media. Changes induced by SnO_2, NiO and SnO_2/NiO mixed-oxide nanoparticles, J. Fluor. 26 (2016) 217.
[43] D. Haridas, A. Chowdhuri, K. Sreenivas, V. Gupta, Effect of thickness of platinum catalyst clusters on response of SnO_2 thin film sensor for LPG, Sens. Actuators B: Chem. 153 (2011) 89.
[44] J. Yang, T. Xie, C. Liu, L. Xu, Facile fabrication of dumbbell-like β-Bi_2O_3/graphene nanocomposites and their highly efficient photocatalytic activity, Materials 11 (2018) 1359.
[45] P.A. Luque, O. Nava, C.A. Soto-Robles, H.E. Garrafa-Galvez, M.E. Martinez-Rosas, M.J. Chinchilas-Chinchillas, A.R. Vilchis-Nestor, A. Castro-Beltran, SnO_2 nanoparticles synthesized with Citrus aurantifolia and their performance in photocatalysis, J. Mater. Sci. Mater. Electron 31 (2020) 16859.
[46] S. Suthakaran, S. Dhanapandian, N. Krishnakumar, N. Ponpandian, Hydrothermal synthesis of SnO_2 nanoparticles and its photocatalytic degradation of methyl violet and electrochemical performance, Mater. Res. Express 6 (2019) 0850i3.
[47] S. Anitha, A.R. Balu, S. Balamurugan, M. Suganya, Z. Delci, M. Karthika, C. Kayathiri, S.C. Devi, A comparative study on the photocatalytic performance of two third order NLO active nanocomposites (NiO-CdO and NiO-CuO) green synthesized using Psidium guajava leaf extract, Inorg. Chem. Commun. 134 (2021) 109073.
[48] W. Yan, X. Zeng, G. Wu, W. Jiang, D. Wei, M. Ling, H. Zhou, C. Guo, Raspberry-like hollow SnO_2-based nanostructures for sensing VOCs and ammonia, J. Mater. Sci. Mater. Electron. 31 (2020) 14165.
[49] T. Mahmoudi, W.-Y. Rho, M. Kohan, Y.H. Im, S. Mathur, Y.-B. Hahn, Suppression of Sn^{2+}/Sn^{4+} oxidation in tin-based perovskite solar cells with graphene-tin quantum dots composites in active layer, Nano Energy 90 (2021) 106495.
[50] A. Stanoiu, A.C. Kuncser, D. Ghica, O.G. Florea, S. Somacescu, C.E. Simion, Sensing properties of NiO loaded SnO_2 nanoparticles-Specific selectivity to H_2S, Chemosensors 9 (2021) 125.
[51] P.G. Choi, N. Izu, N. Shirahata, Y. Masuda, SnO_2 nanosheets for selective alkene gas sensing, ACS Appl. Nano Mater. 2 (2019) 1820.
[52] W. Huang, S. Ding, Y. Chen, W. Hao, X. Lai, J. Peng, J. Tu, Y. Cao, X. Li, 3D NiO hollow sphere/reduced graphene oxide composite for high-performance glucose biosensor, Sci. Rep. 7 (2017) 5220.
[53] X.M.C. Ta, T.K.A. Nguyen, A.D. Bui, H.T. Nguyen, R. Daiyan, R. Amal, T. Tran-Phu, A. Tricoli, Optimizing surface composition and structure of $FeWO_4$ photoanodes for enhanced water photooxidation, Adv. Mater. Technol. 8 (2023) 2201760.
[54] A. Agresti, A. Pazniak, S. Pescetelli, A.D. Vito, D. Rossi, A. Pecchia, M. Auf der Maur, A. Liedl, R. Larciprete, D.V. Kuznetsov, D. Saranin, A.D. Carlo, Titanium-carbide MXenes for work function and interface engineering in perovskite solar cells, Nat. Mater. 18 (2019) 1228.
[55] C. Zhao, C.G. Tang, Z.-L. Seah, Q.-M. Koh, L.-L. Chua, R.-Q. Png, P.K.H. Ho, Improving organic photovoltaic cells by forcing electrode work function well beyond onset of ohmic transition, Nat. Commun. 12 (2021) 2250.

Jihyun Lee received a Bachelor's degree in Material Science and Engineering at Kookmin University in 2020. Since 2020, she is currently a Ph.D. candidate at the Department of Materials Science and Engineering at Yonsei University under the supervision of Prof. Wooyoung Lee. She is currently studying on nanostructured metal-oxide semiconductor gas sensors.

Yu Jin Kim is a research professor in the Department of Materials Science and Engineering and a research institute of the Korea Initiative for Fostering University of Research and Innovation (KIURI). She received a Ph.D. degree from Pohang University of Science and Technology (POSTECH) in 2016 and started to work at Argonne National Laboratory as a Named-fellowship post-doc in the same year. From the end of 2019, she worked at Argonne as an assistant scientist in the Center for Nanoscale Materials and Argonne Photon Source. After 2 years, she moved to SLAC national accelerator laboratory and worked at Stanford Synchrotron Radiation Laboratory. She has expertize in X-ray science to investigate the internal information of semiconducting materials. Currently, she has mainly focused on the discovery of a sensing mechanism in sensor devices.

Wooyoung Lee is the Underwood distinguished professor of the Department of Materials Science and Engineering at Yonsei University in Korea. He is also the Director of the Center for Super Critical Material Industrial Technology, National Core Materials Research Center and the institute of Korea Initiative for Fostering University of Research and Innovation. He is the President of The Korean Magnetics Society and a regular member of the National Academy of Engineering of Korea. In recent years, his research interests have centered on hydrogen sensors, various metal oxide semiconducting gas sensors, and breath analyzers. He is also studying rare-earth permanent magnets and thermoelectric materials and devices. He has received a number of awards in nano-related research areas including a Prime Minister Award (2023) in Nano Korea 2023, SeAH-Haiam Fellowship Award (2018) in The Korean Institute of Metals and Materials and a Service Merit Medal (2008) from the Government of Korea due to his contribution to the development of intellectual properties. He has authored and co-authored over 280 publications and has edited three special books on nanostructured materials and devices.